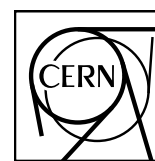




TOTEM 2012-002  
14 August 2012



CERN-PH-EP-2012-239  
17 August 2012

**Measurement of proton-proton elastic scattering and total cross-section at  
 $\sqrt{s} = 7 \text{ TeV}$**

The TOTEM Collaboration

G. Antchev<sup>a)</sup>, P. Aspell<sup>8)</sup>, I. Atanassov<sup>8,a)</sup>, V. Avati<sup>8)</sup>, J. Baechler<sup>8)</sup>, V. Berardi<sup>5b,5a)</sup>, M. Berretti<sup>7b)</sup>,  
E. Bossini<sup>7b)</sup>, M. Bozzo<sup>6b,6a)</sup>, P. Brogi<sup>7b)</sup>, E. Brücken<sup>3a,3b)</sup>, A. Buzzo<sup>6a)</sup>, F. S. Cafagna<sup>5a)</sup>,  
M. Calicchio<sup>5b,5a)</sup>, M. G. Catanesi<sup>5a)</sup>, C. Covault<sup>9)</sup>, M. Csanád<sup>4,e)</sup>, T. Csörgő<sup>4)</sup>, M. Deile<sup>8)</sup>, K. Eggert<sup>9)</sup>,  
V. Eremin<sup>b)</sup>, R. Ferretti<sup>6a,6b)</sup>, F. Ferro<sup>6a)</sup>, A. Fiergolski<sup>c)</sup>, F. Garcia<sup>3a)</sup>, S. Giani<sup>8)</sup>, V. Greco<sup>7b,8)</sup>,  
L. Grzanka<sup>8,d)</sup>, J. Heino<sup>3a)</sup>, T. Hilden<sup>3a,3b)</sup>, R. A. Intonti<sup>5a)</sup>, J. Kašpar<sup>1a,8)</sup>, J. Kopal<sup>1a,8)</sup>, V. Kundrať<sup>1a)</sup>,  
K. Kurvinen<sup>3a)</sup>, S. Lami<sup>7a)</sup>, G. Latino<sup>7b)</sup>, R. Lauhakangas<sup>3a)</sup>, T. Leszko<sup>c)</sup>, E. Lippmaa<sup>2)</sup>,  
M. Lokajčiček<sup>1a)</sup>, M. Lo Vetere<sup>6b,6a)</sup>, F. Lucas Rodríguez<sup>8)</sup>, M. Macri<sup>6a)</sup>, T. Mäki<sup>3a)</sup>,  
A. Mercadante<sup>5b,5a)</sup>, N. Minafra<sup>8)</sup>, S. Minutoli<sup>6a)</sup>, F. Nemes<sup>4,e)</sup>, H. Niewiadomski<sup>8)</sup>, E. Oliveri<sup>7b)</sup>,  
F. Oljemark<sup>3a,3b)</sup>, R. Orava<sup>3a,3b)</sup>, M. Oriunno<sup>8,f)</sup>, K. Österberg<sup>3a,3b)</sup>, P. Palazzi<sup>7b)</sup>, J. Procházka<sup>1a)</sup>,  
M. Quinto<sup>5a)</sup>, E. Radermacher<sup>8)</sup>, E. Radicioni<sup>5a)</sup>, F. Ravotti<sup>8)</sup>, E. Robutti<sup>6a)</sup>, L. Ropelewski<sup>8)</sup>,  
G. Ruggiero<sup>8)</sup>, H. Saarikko<sup>3a,3b)</sup>, A. Santroni<sup>6b,6a)</sup>, A. Scribano<sup>7b)</sup>, J. Smajek<sup>8)</sup>, W. Snoeys<sup>8)</sup>,  
J. Sziklai<sup>4)</sup>, C. Taylor<sup>9)</sup>, N. Turini<sup>7b)</sup>, V. Vacek<sup>1b)</sup>, M. Vitek<sup>1b)</sup>, J. Weiti<sup>3a,3b)</sup> and J. Whitmore<sup>10)</sup>

<sup>1a</sup>Institute of Physics of the Academy of Sciences of the Czech Republic, Praha, Czech Republic, EU

<sup>1b</sup>Czech Technical University, Praha, Czech Republic, EU

<sup>2</sup>National Institute of Chemical Physics and Biophysics NICPB, Tallinn, Estonia, EU

<sup>3a</sup>Helsinki Institute of Physics, Finland, EU

<sup>3b</sup>Department of Physics, University of Helsinki, Finland, EU

<sup>4</sup>MTA Wigner Research Center, RMKI, Budapest, Hungary, EU

<sup>5a</sup>INFN Sezione di Bari, Italy, EU

<sup>5b</sup>Dipartimento Interateneo di Fisica di Bari, Italy, EU

<sup>6a</sup>Sezione INFN, Genova, Italy, EU

<sup>6b</sup>Università degli Studi di Genova, Italy, EU

<sup>7a</sup>INFN Sezione di Pisa, Italy, EU

<sup>7b</sup>Università degli Studi di Siena and Gruppo Collegato INFN di Siena, Italy, EU

<sup>8</sup>CERN, Geneva, Switzerland

<sup>9</sup>Case Western Reserve University, Dept. of Physics, Cleveland, OH, USA

<sup>10</sup>Penn State University, Dept. of Physics, University Park, PA, USA

<sup>a</sup>INRNE-BAS, Institute for Nuclear Research and Nuclear Energy, Bulgarian Academy of Sciences, Sofia, Bulgaria, EU

<sup>b</sup>Ioffe Physical - Technical Institute of Russian Academy of Sciences, St. Petersburg, Russian Federation

<sup>c</sup>Warsaw University of Technology, Poland, EU

<sup>d</sup>Institute of Nuclear Physics, Polish Academy of Science, Cracow, Poland, EU

<sup>e</sup>Department of Atomic Physics, Eötvös University, Hungary, EU

<sup>f</sup>SLAC National Accelerator Laboratory, Stanford CA, USA

## Abstract

At the LHC energy of  $\sqrt{s} = 7 \text{ TeV}$ , under various beam and background conditions, luminosities, and Roman Pot positions, TOTEM has measured the differential cross-section for proton-proton elastic scattering as a function of the four-momentum transfer squared  $t$ . The results of the different analyses are in excellent agreement demonstrating no sizeable dependence on the beam conditions. Due to the very close approach of the Roman Pot detectors to the beam center ( $\approx 5\sigma_{\text{beam}}$ ) in a dedicated run with  $\beta^* = 90 \text{ m}$ ,  $|t|$ -values down to  $5 \cdot 10^{-3} \text{ GeV}^2$  were reached. The exponential slope of the differential elastic cross-section in this newly explored  $|t|$ -region remained unchanged and thus an exponential fit with only one constant  $B = (19.9 \pm 0.3) \text{ GeV}^{-2}$  over the large  $|t|$ -range from 0.005 to  $0.2 \text{ GeV}^2$  describes the differential distribution well. The high precision of the measurement and the large fit range lead to an error on the slope parameter  $B$  which is remarkably small compared to previous experiments. It allows a precise extrapolation over the non-visible cross-section (only 9%) to  $t = 0$ . With the luminosity from CMS, the elastic cross-section was determined to be  $(25.4 \pm 1.1) \text{ mb}$ , and using in addition the optical theorem, the total pp cross-section was derived to be  $(98.6 \pm 2.2) \text{ mb}$ . For model comparisons the  $t$ -distributions are tabulated including the large  $|t|$ -range of the previous measurement [1].

## 1 Introduction

The study of elastic proton-proton scattering reveals many aspects about the structure of the proton, its shape and opacity, i.e. matter density. It also tests the interplay of non-perturbative and perturbative regimes of pp interactions depending on the four-momentum transfer squared  $t$  involved in the scattering process.

In several runs with different beam optics, TOTEM has measured at the center-of-mass energy of 7 TeV the differential elastic cross-section  $d\sigma/dt$  over a wide range of  $t$ . The first measurement, reported by the TOTEM collaboration [1], covered the  $|t|$ -range from 0.36 to 2.5 GeV<sup>2</sup>. These data were taken with the standard 2010 LHC beam optics (with the betatron value at the intersection point  $\beta^*$  of 3.5 m). The differential cross-section  $d\sigma/dt$  exhibited an exponential decay at low  $|t|$  followed by a significant diffractive minimum and at larger  $|t|$ -values a behavior compatible with the power law already observed at lower energies (see references 1 to 11 in [1]).

To access smaller  $|t|$ -values (at  $\sqrt{s} = 7\text{ TeV}$   $|t| = 0.01\text{ GeV}^2$  corresponds to a scattering angle of  $\approx 29\ \mu\text{rad}$ ) the colliding beams must have a beam divergence of a few micro-radians. This can be obtained by either increasing the betatron value  $\beta^*$  or by reducing the beam emittance  $\varepsilon$  (beam divergence =  $\sqrt{\varepsilon/\beta^*}$ ). With a dedicated beam optics configuration ( $\beta^* = 90\text{ m}$ ), TOTEM extended the measurement to  $|t|$ -values as low as  $2 \cdot 10^{-2}\text{ GeV}^2$  [2]. This made the extrapolation of the differential cross-section to the optical point at  $t = 0$  possible and enabled, for the first time at the LHC, the determination of the elastic scattering cross-section as well as the total cross-section via the optical theorem.

This article presents an improved  $t$ -distribution measurement with higher statistics and a reach to even smaller  $|t|$ -values using different data sets taken in October 2011, with several special runs at  $\beta^* = 90\text{ m}$ . This time, the detectors, housed in Roman Pots (RP), were put very close to the beam center: 4.8 to 6.5 times the transverse beam size  $\sigma_{\text{beam}}$ . This was possible since the beams were scraped by the LHC collimators at a distance of  $4\sigma_{\text{beam}}$  for RP alignment purposes. For the definition of their position, each Roman Pot was brought to touch this sharp beam edge. After retraction by 0.5 to  $2\sigma_{\text{beam}}$ , TOTEM took data in very clean conditions with only a few colliding bunch pairs and reached  $|t|$  values down to  $5 \cdot 10^{-3}\text{ GeV}^2$ , enabling the observation of 91% of the elastic cross-section – compared to only 67% previously [2]. By extrapolating the differential elastic cross-section to the optical point  $t = 0$  and using the optical theorem, the total and inelastic cross-sections were also derived. The differential cross-section over the complete  $t$ -range combining all available measurements with its statistical and systematic uncertainties is tabulated in this article.

In the same journal issue, a direct inelastic cross-section measurement, based on triggers from the forward inelastic detectors, is reported [3]. This is compared to the inelastic cross-section obtained from elastic scattering via the optical theorem, yielding a cross-section estimate for single diffraction at masses below 3.4 GeV that escape our detection. Another article [4] summarizes the cross-sections obtained with different approaches, including the luminosity independent method. Since the  $\rho$  parameter (the ratio of the real to imaginary part of the hadronic scattering amplitude at  $t = 0$ ) does not enter in the method from Ref. [3],  $\rho$  can be determined by comparing the results from the different methods. Furthermore, the luminosity of the LHC was extracted, confirming the more detector-dependent estimates by CMS.

## 2 The proton detectors

The configuration of the TOTEM Roman Pot system and the silicon detector properties have already been described in detail [5, 1, 2]. For the understanding of the analysis, a few basic system properties are repeated.

The silicon sensors are placed in movable beam-pipe insertions – Roman Pots – located symmetrically on both sides of the LHC interaction point (IP) 5 at distances of 215 – 220 m from the IP.

Each RP station is composed of two units (near and far) separated by a distance of about 5 m. A unit consists of 3 RPs, two approaching the outgoing beam vertically from the top and the bottom and one horizontally. Each RP is equipped with a stack of 10 silicon strip detectors measuring the proton distance to the beam center in both coordinates perpendicular to the beam with a precision of about  $11 \mu\text{m}$ . The movement and the alignment of all pots are monitored with a precision better than  $20 \mu\text{m}$  based on track reconstruction and external alignment tools.

The large lever arm between the near and the far units allows the determination of the track angle in both projections with a precision of about  $5 \mu\text{rad}$ . The knowledge of both the track positions and angles is vital in the analysis.

### 3 LHC Optics

The measurement presented in this article was performed with the  $\beta^* = 90\text{m}$  optics, which has been described in detail [2]; here we repeat only the most important properties. A proton elastically scattered at the vertex ( $x^*, y^*, z^* = 0$ ) with the horizontal and vertical scattering angles ( $\theta_x^*, \theta_y^*$ ) is transported through the LHC magnet lattice and traverses the Roman Pots at points  $(x, y)$ :

$$\begin{aligned} x &= L_x \theta_x^* + v_x x^* & , & & y &= L_y \theta_y^* + v_y y^* \\ L_x &= 2.9\text{m (near)} & , & & L_y &= 240\text{m (near)} \\ L_x &\approx 0\text{m (far)} & , & & L_y &= 260\text{m (far)} . \end{aligned} \quad (1)$$

Since  $L_x \approx 0$  in the far RP, the corresponding horizontal hit position  $x^F$  can be used for the vertex  $x^*$  determination:

$$x^* = \frac{x^F}{v_x} . \quad (2)$$

The optimal scattering-angle reconstruction formulae differ for the two projections: the vertical angle  $\theta_y^*$  is reconstructed from the hit position  $y$  (since  $v_y \approx 0$ ) while the horizontal angle  $\theta_x^*$  from the track angle  $\theta_x$  at the RP:

$$\theta_y^* = \frac{y}{L_y} , \quad \theta_x^* = \frac{1}{\frac{dL_x}{ds}} \left( \theta_x - \frac{dv_x}{ds} x^* \right) , \quad (3)$$

where  $s$  denotes the distance from the interaction point.

### 4 Data taking

The presented data were recorded in October 2011. For this analysis, only one colliding bunch-pair was used with an average proton population of  $6 \cdot 10^{10}$  protons/bunch producing an instantaneous luminosity of  $6\text{mb}^{-1}\text{s}^{-1}$  and an average inelastic-interaction rate of 0.03 per bunch crossing.

During the run three data sets were recorded with different RP distances to the beam center corresponding to minimum values of the four-momentum transfer squared between  $(4.6 \text{ and } 7.3) \cdot 10^{-3} \text{GeV}^2$ . The different data sets enabled to reduce certain systematic uncertainties (alignment, inefficiency corrections, etc.). A run summary is given in Tab. 1.

The first-level trigger benefits from the 20 possible hits (10 planes in both near and far RP) per proton track and is based on a track segment in the near or the far unit. This redundancy guarantees a high trigger efficiency (over 99% per proton). A coincidence between a proton on the left and the right side of the IP is requested in the elastic double-arm signature in the vertical RP detectors with two diagonals (left top – right bottom or left bottom – right top). The characteristics of the  $\beta^* = 90\text{m}$  optics force most of the elastically scattered protons into the vertical RPs, see Fig. 1.

**Table 1:** Description of the three datasets available. The RP position gives the RP approach to the beam in multiples of the beam size ( $\sigma_{\text{beam}}$ ). The third column summarizes the numbers of elastic events reconstructed from both diagonals.  $\mathcal{L}_{\text{int}}$  is the integrated luminosity for each dataset, accounting for the data-acquisition (DAQ) inefficiency. The last column shows the lowest  $|t|$  values reached.

dataset	RP position	elastic events	$\mathcal{L}_{\text{int}}$ [ $\mu\text{b}^{-1}$ ]	$ t _{\text{min}}$ [ $\text{GeV}^2$ ]
1	$6.5 \sigma_{\text{beam}}$	841k	68.0	$7.3 \cdot 10^{-3}$
2	$5.5 \sigma_{\text{beam}}$	106k	8.2	$5.7 \cdot 10^{-3}$
3	$4.8 \sigma_{\text{beam}}$	89k	6.6	$4.6 \cdot 10^{-3}$

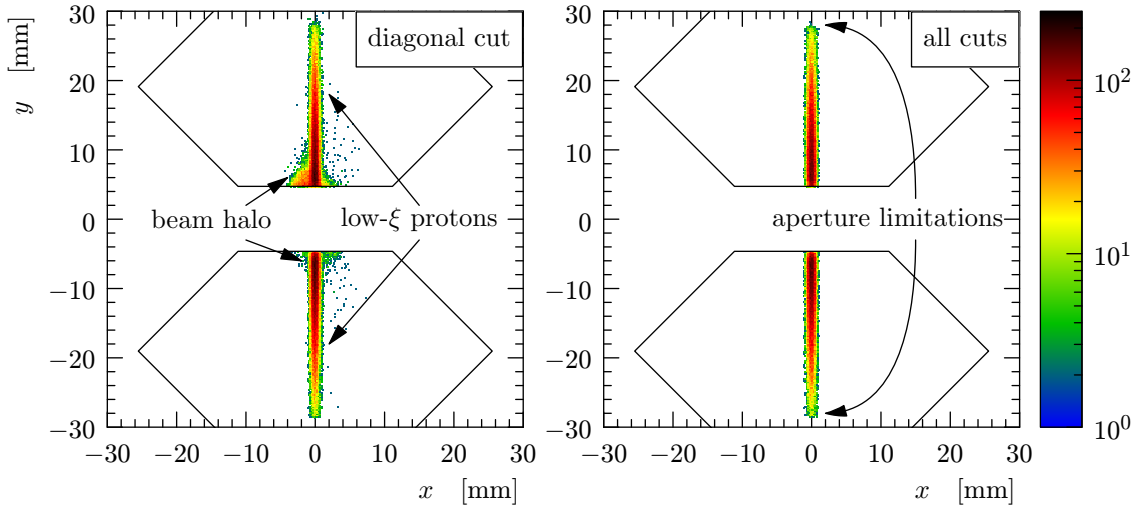


**Fig. 1:** Hit distributions from dataset 3 in the far unit of the 220m station, right arm. Left: with diagonal cut only, Right: with all the elastic selection cuts (see Tab. 2). The left plot clearly shows the presence of a beam halo, which is eliminated by the selection cuts (right plot). The distribution of elastic hits in the right plot is sharply cut at about  $|y| = 29\text{mm}$  as a consequence of the LHC aperture limitations.

**Table 2:** The elastic selection cuts. The superscripts R and L refer to the right and left arm, the N and F corresponds to the near and far units. The constant  $\alpha = L_y^F/L_y^N - 1 \approx 0.11$ . The right-most column gives the RMS of the cut distribution ( $\equiv 1\sigma$ ), all the cuts are applied at  $3\sigma$ -level.

number	cut	RMS
diagonal	track reconstructed in all 4 diagonal RPs	
1	$\theta_x^{*R} - \theta_x^{*L}$	$9.2 \mu\text{rad}$
2	$\theta_y^{*R} - \theta_y^{*L}$	$3.5 \mu\text{rad}$
3	$ x^{*R} $	$200 \mu\text{m}$
4	$ x^{*L} $	$200 \mu\text{m}$
5	$\alpha y^{R,N} - (y^{R,F} - y^{R,N})$	$17 \mu\text{m}$
6	$\alpha y^{L,N} - (y^{L,F} - y^{L,N})$	$17 \mu\text{m}$
7	$x^{*R} - x^{*L}$	$9 \mu\text{m}$

## 5 Analysis

The analysis is very similar to the previous one [2]. Here, advantage was taken of having three datasets (each with two diagonals) analyzed separately, thus leading to a better control over the systematics.

### 5.1 Alignment

Three complementary methods were applied [6]. First, the RP position was approximately given by the beam-based alignment [7]. Second, proton tracks passing through the overlap between the vertical and horizontal RPs were used to determine the relative alignment of the RPs of each unit. Third, since the elastic event tagging does not require a precise alignment, an alignment fine-tuning was performed on a sample obtained from a pre-selection of elastic events (see next paragraph). By exploiting the azimuthal symmetry of elastic scattering, the horizontal and vertical shifts and the tilt of each unit could be adjusted. The effect of residual misalignments on  $d\sigma_{el}/dt$  was thus smaller than 0.3% for every  $t$ -bin.

### 5.2 Elastic tagging

The cuts used to select the elastic events are summarized in Tab. 2. Cuts 1 and 2 require the reconstructed-track collinearity between the left and right arm. Cuts 3 to 6 effectively work as low- $\xi$  cuts ( $\xi$  being the fractional momentum loss of a proton). Cuts 3 and 4: if  $\xi \neq 0$ , the vertex reconstruction in Eq. (2) becomes invalid. Cuts 5 and 6: if  $\xi \neq 0$ , the correlation between the track position ( $y^N$ ) and the track angle (proportional to  $y^F - y^N$ ) is lost. Cut 7 compares the horizontal vertex position reconstructed from the left and right arms. It is the strongest single cut and is very effective against the beam-halo background, see Fig. 1.

### 5.3 Kinematics reconstruction

The scattering angles were reconstructed for each arm according to Eq. (3). The corresponding uncertainties were 1.3% and 0.8% for  $\theta_x^*$  and  $\theta_y^*$ , respectively. The former has a more pronounced effect on  $d\sigma_{el}/dt$  and is the leading systematic uncertainty for larger  $|t|$  values, cf. Tab. 3.

For elastic events, the angles reconstructed from left and right arms were averaged, which leads to an uncertainty reduction.

### 5.4 Background

The background contribution (i.e. all non-elastic events passing the selection cuts) was estimated by omitting the strongest single cut (number 7 in Tab. 2) and by analyzing the distribution of  $x^{*R} - x^{*L}$ . This distribution can be reasonably described by two Gaussians – one for the signal and one for the

background. By interpolating the background tails ( $|\Delta x^*| > 3\sigma$ ) into the signal region ( $|\Delta x^*| < 3\sigma$ ), the background/signal ratio was determined as  $(0.8 \pm 0.4)\%$ .

### 5.5 Acceptance correction

Two acceptance limitations were identified: the detector edge (relevant for low  $|t|$ ) and the LHC aperture limitation shown in Fig. 1, right (relevant for high  $|t|$ ). Both effects were treated by assuming azimuthal symmetry of the elastic scattering and by correcting for smearing around the limitation edges. In order to keep the uncertainty at a reasonable level, the analysis was constrained into the region where the full acceptance correction was not larger than a factor 7.5.

### 5.6 Unfolding of resolution effects

The angular resolution was determined by comparing the scattering angles reconstructed from the left and right arm. Combining all the three datasets and all the diagonals yields one-arm resolutions of  $(6.36 \pm 0.21)\mu\text{rad}$  in  $\theta_x^*$  and  $(2.47 \pm 0.07)\mu\text{rad}$  in  $\theta_y^*$ . The latter is predominantly due to the beam-divergence, whereas the  $\theta_x^*$  resolution is deteriorated by a contribution from the finite detector pitch.

The  $t$ -resolution impact on  $d\sigma_{\text{el}}/dt$  was determined (and eliminated) by an iterative procedure, that starts by taking the observed (smeared)  $t$ -distribution as an input to a Monte-Carlo calculation of the un-smearing correction. The correction is applied to the observed  $t$ -distribution and yields a better estimate of the true  $t$ -distribution. These two steps were repeated three times to reach convergence. The systematic uncertainty of this procedure (due to the uncertainty of the  $\theta_{x,y}^*$  resolution) was estimated to be smaller than 0.5%.

### 5.7 Efficiencies

The efficiency of the RP trigger was estimated by using the zero-bias data stream. The selection of elastic events was repeated for these data and the RP trigger was found efficient for all the selected events. Therefore, at 68% confidence level, it was concluded that the trigger efficiency was higher than 99.8%.

The DAQ inefficiency (dead time) was determined by comparing the numbers of triggered and recorded events, yielding  $(1.858 \pm 0.001)\%$ .

Reconstruction inefficiencies occur due to: intrinsic RP detection inefficiency of each silicon sensor, proton interactions with the material of a RP and “pile-up” of several protons in one event (RPs can uniquely reconstruct only one track). For the last case, the most important contribution is a coincidence of an elastic proton and a beam-halo proton, see Fig. 1.

Uncorrelated inefficiencies of separate RPs were studied by removing the RP in question from the selection cuts and counting the recovered events. For this study, only cut 2 could be kept – the others require both near and far RP measurements. The result was an inefficiency of  $(1.5 \pm 0.2)\%$  for the near and  $(3.0 \pm 0.2)\%$  for the far RPs. This difference can be explained by the proton interactions in the near RP that affect the far RP too. This near-far correlated inefficiency was determined from data by counting events with corresponding shower signatures, yielding  $(1.5 \pm 0.7)\%$  (this result is confirmed by MC simulations).

The “pile-up” inefficiency was calculated from the probability of finding an additional track (on top of the elastic) in any station of a diagonal. This probability was determined from the zero-bias data stream and was found to increase as the RPs approached the beam. For instance, for the diagonal bottom-left top-right, the probabilities were  $(3.9 \pm 0.3)\%$ ,  $(6.2 \pm 0.3)\%$  and  $(7.9 \pm 0.3)\%$  for the datasets 1, 2 and 3, respectively.

**Table 3:** Overview of the systematic uncertainties of the differential cross-section  $d\sigma_{\text{el}}/dt$ .

$ t $ [GeV <sup>2</sup> ]	$t$ -dependent	normalization	luminosity	total
0.005	1.8%	.	.	4.5%
0.01	1.0%	.	.	4.3%
0.06	0.3%	.	.	4.2%
0.1	0.9%	.	.	4.3%
0.12	1.2%	1.2%	4.0%	4.3%
0.16	3.0%	.	.	5.1%
0.2	4.4%	.	.	6.1%
0.3	8.3%	.	.	9.3%
0.4	12.3%	.	.	12.9%

## 5.8 Luminosity

In this paper, the luminosity measured by CMS (with a 4%-uncertainty estimate) was used. Luminosity-independent results are given elsewhere [4].

## 6 Systematic uncertainty calculation

For each of the analysis steps above, the systematic uncertainty effect on  $d\sigma_{\text{el}}/dt$  was estimated with a Monte-Carlo simulation. Tab. 3 summarizes these uncertainties for several  $|t|$  values, grouping the contributions into three categories:  $t$ -dependent,  $t$ -independent (normalization) and luminosity uncertainties. Since there are a number of contributions in each category, the uncertainties were combined in quadrature.

The luminosity uncertainty is the leading systematic effect for  $|t| < 0.2 \text{ GeV}^2$ , above that point it is the uncertainty of  $dL_x/ds$ . The optics-related error contribution is almost vanishing around  $|t| = 0.06 \text{ GeV}^2$  and has opposite signs below and above that point. Therefore there is a partial error cancellation in the integrated elastic cross-section  $\sigma_{\text{el}}$ , and consequently the relative error of  $\sigma_{\text{el}}$  is significantly lower than the one of  $d\sigma_{\text{el}}/dt|_0$  – see Tab. 7. Moreover, there is a strong correlation between the errors of  $\sigma_{\text{el}}$  and  $d\sigma_{\text{el}}/dt|_0$  – the correlation coefficient is 0.76.

## 7 Extrapolation to $t = 0$

The measured differential cross-section can be well ( $\chi^2/\text{n.d.f.} \approx 1.2$ ) described with the parameterization

$$\frac{d\sigma_{\text{el}}}{dt} = \frac{d\sigma_{\text{el}}}{dt} \Big|_{t=0} e^{-B|t|} \quad (4)$$

over a large  $|t|$ -range, see Tab. 6 and the black line in Fig. 2. Since the slope  $B$  remains constant even for the lowest  $|t|$  values, one may conclude that the effects of the Coulomb-hadronic interference (for details see, e.g., [8]) are smaller than our experimental sensitivity. Therefore, within the uncertainties, the fit can be attributed to the hadronic component of the scattering amplitude. Furthermore, it is assumed that Eq. (4) describes the hadronic cross-section also for  $|t|$  values below our acceptance and thus the fit can be used in the optical theorem to calculate the total cross-section according to Eq. (5).

## 8 Results

TOTEM has taken data under various beam and background conditions, luminosities and RP detector positions. The differential elastic cross-section obtained from these different data sets are in excellent



**Table 4:** The elastic differential cross-section determined in this analysis. Some details on the systematic uncertainty calculation can be found in Tab. 3, which can also be used to evaluate the correlations of the systematic uncertainties among the bins (the three contributions are independent).

$ t $ [GeV <sup>2</sup> ]	$\frac{d\sigma_{el}}{dt}$ [mb/GeV <sup>2</sup> ]	$\pm$ stat $\pm$ syst	$ t $ [GeV <sup>2</sup> ]	$\frac{d\sigma_{el}}{dt}$ [mb/GeV <sup>2</sup> ]	$\pm$ stat $\pm$ syst	$ t $ [GeV <sup>2</sup> ]	$\frac{d\sigma_{el}}{dt}$ [mb/GeV <sup>2</sup> ]	$\pm$ stat $\pm$ syst	$ t $ [GeV <sup>2</sup> ]	$\frac{d\sigma_{el}}{dt}$ [mb/GeV <sup>2</sup> ]	$\pm$ stat $\pm$ syst
0.00515	465.	$\pm 27.$ $\pm 21.$	0.0477	197.2	$\pm 1.3$ $\pm 8.3$	0.106	61.90 $\pm 0.58$ $\pm 2.66$		0.196	10.11	$\pm 0.23$ $\pm 0.61$
0.00650	465.	$\pm 11.$ $\pm 21.$	0.0499	187.5	$\pm 1.3$ $\pm 7.9$	0.109	58.11 $\pm 0.55$ $\pm 2.50$		0.201	9.31	$\pm 0.22$ $\pm 0.57$
0.00818	437.5 $\pm$	5.0 $\pm 19.1$	0.0522	178.1	$\pm 1.2$ $\pm 7.5$	0.112	54.11 $\pm 0.53$ $\pm 2.33$		0.207	8.07	$\pm 0.21$ $\pm 0.51$
0.00995	411.0 $\pm$	3.3 $\pm 17.7$	0.0545	168.8	$\pm 1.2$ $\pm 7.1$	0.116	51.21 $\pm 0.51$ $\pm 2.20$		0.213	6.98	$\pm 0.19$ $\pm 0.45$
0.0117	402.3 $\pm$	2.9 $\pm 17.3$	0.0569	162.5	$\pm 1.1$ $\pm 6.8$	0.119	48.24 $\pm 0.49$ $\pm 2.07$		0.219	6.22	$\pm 0.17$ $\pm 0.42$
0.0135	384.5 $\pm$	2.6 $\pm 16.5$	0.0592	155.5	$\pm 1.1$ $\pm 6.5$	0.122	44.99 $\pm 0.46$ $\pm 1.96$		0.225	5.38	$\pm 0.16$ $\pm 0.37$
0.0154	378.0 $\pm$	2.4 $\pm 16.2$	0.0616	149.4	$\pm 1.1$ $\pm 6.3$	0.126	42.74 $\pm 0.45$ $\pm 1.89$		0.232	4.40	$\pm 0.14$ $\pm 0.31$
0.0172	360.3 $\pm$	2.3 $\pm 15.4$	0.0641	140.2	$\pm 1.0$ $\pm 5.9$	0.130	39.49 $\pm 0.43$ $\pm 1.77$		0.239	4.25	$\pm 0.14$ $\pm 0.31$
0.0191	348.1 $\pm$	2.2 $\pm 14.9$	0.0666	135.10 $\pm 0.99$	$\pm 5.70$	0.133	35.75 $\pm 0.43$ $\pm 1.63$		0.246	3.47	$\pm 0.13$ $\pm 0.26$
0.0210	337.0 $\pm$	2.1 $\pm 14.4$	0.0691	129.00 $\pm 0.96$	$\pm 5.45$	0.137	33.63 $\pm 0.41$ $\pm 1.56$		0.253	2.82	$\pm 0.11$ $\pm 0.22$
0.0229	325.0 $\pm$	2.0 $\pm 13.9$	0.0716	120.53 $\pm 0.91$	$\pm 5.10$	0.141	31.08 $\pm 0.41$ $\pm 1.47$		0.261	2.52	$\pm 0.10$ $\pm 0.20$
0.0248	307.9 $\pm$	1.9 $\pm 13.1$	0.0742	115.10 $\pm 0.89$	$\pm 4.88$	0.145	28.91 $\pm 0.39$ $\pm 1.39$		0.270	2.142 $\pm 0.097$	$\pm 0.178$
0.0268	296.7 $\pm$	1.8 $\pm 12.7$	0.0769	109.63 $\pm 0.86$	$\pm 4.65$	0.149	25.65 $\pm 0.38$ $\pm 1.25$		0.278	1.824 $\pm 0.086$	$\pm 0.157$
0.0287	285.9 $\pm$	1.8 $\pm 12.2$	0.0795	104.97 $\pm 0.83$	$\pm 4.46$	0.153	24.16 $\pm 0.36$ $\pm 1.20$		0.287	1.455 $\pm 0.075$	$\pm 0.129$
0.0307	275.3 $\pm$	1.7 $\pm 11.7$	0.0823	100.22 $\pm 0.80$	$\pm 4.27$	0.157	22.35 $\pm 0.35$ $\pm 1.13$		0.297	1.257 $\pm 0.069$	$\pm 0.116$
0.0328	263.0 $\pm$	1.6 $\pm 11.2$	0.0850	93.18 $\pm 0.76$	$\pm 3.97$	0.162	20.22 $\pm 0.34$ $\pm 1.04$		0.307	0.848 $\pm 0.055$	$\pm 0.081$
0.0348	252.0 $\pm$	1.6 $\pm 10.7$	0.0878	89.16 $\pm 0.74$	$\pm 3.81$	0.166	19.01 $\pm 0.32$ $\pm 1.00$		0.318	0.633 $\pm 0.046$	$\pm 0.063$
0.0369	242.8 $\pm$	1.5 $\pm 10.3$	0.0907	81.78 $\pm 0.70$	$\pm 3.50$	0.171	16.92 $\pm 0.30$ $\pm 0.91$		0.330	0.558 $\pm 0.043$	$\pm 0.058$
0.0390	231.6 $\pm$	1.5 $\pm 9.8$	0.0936	78.85 $\pm 0.68$	$\pm 3.38$	0.175	15.20 $\pm 0.29$ $\pm 0.83$		0.342	0.417 $\pm 0.038$	$\pm 0.045$
0.0411	222.2 $\pm$	1.4 $\pm 9.4$	0.0966	73.92 $\pm 0.65$	$\pm 3.17$	0.180	13.90 $\pm 0.28$ $\pm 0.78$		0.356	0.269 $\pm 0.027$	$\pm 0.030$
0.0433	210.9 $\pm$	1.4 $\pm 8.9$	0.0996	68.77 $\pm 0.62$	$\pm 2.96$	0.185	12.09 $\pm 0.26$ $\pm 0.69$		0.371	0.235 $\pm 0.025$	$\pm 0.028$
0.0455	204.8 $\pm$	1.3 $\pm 8.7$	0.103	65.53 $\pm 0.60$	$\pm 2.82$	0.190	11.26 $\pm 0.25$ $\pm 0.66$				

agreement with each other. This justifies merging the data from all datasets to obtain a final result for the differential cross-sections presented in Tab. 4. The first two bins suffer from the lower statistics of the datasets 2 and 3. Tab. 4 gives a representative  $|t|$ -value for each bin, determined according to the procedure described elsewhere [10]. The relative uncertainties of the representative points turn out to be negligible ( $< 10^{-4}$ ). Tab. 5 presents the  $d\sigma_{el}/dt$  continuation to higher  $|t|$  values, measured in a different run with  $\beta^* = 3.5\text{m}$  optics and published elsewhere [1]. All TOTEM differential cross-section measurements are given in Fig. 2.

For  $|t|$ -values below  $0.2\text{GeV}^2$ , the differential cross-section falls exponentially with  $|t|$ , as expressed in Eq. (4). Due to the closer approach of the RP detectors to the beam center (see Tab. 1) in these data, the minimal reachable  $|t|$ -value was lowered from 0.02 of the previous measurement [2] down to  $0.005\text{GeV}^2$ . However, the exponential slope  $B$  of the differential elastic cross-section stayed unchanged in this newly explored  $|t|$ -region. As presented in Tab. 6, the slope does not change with the chosen fit intervals. Consequently, the exponential dependence can be fitted over the large  $|t|$ -interval from  $0.005$  to  $0.2\text{GeV}^2$  resulting in a high precision determination of  $B$ . Compared to previous collider experiments at lower energies (Fig. 3),  $B$  rises steadily with the collision energy  $\sqrt{s}$ .

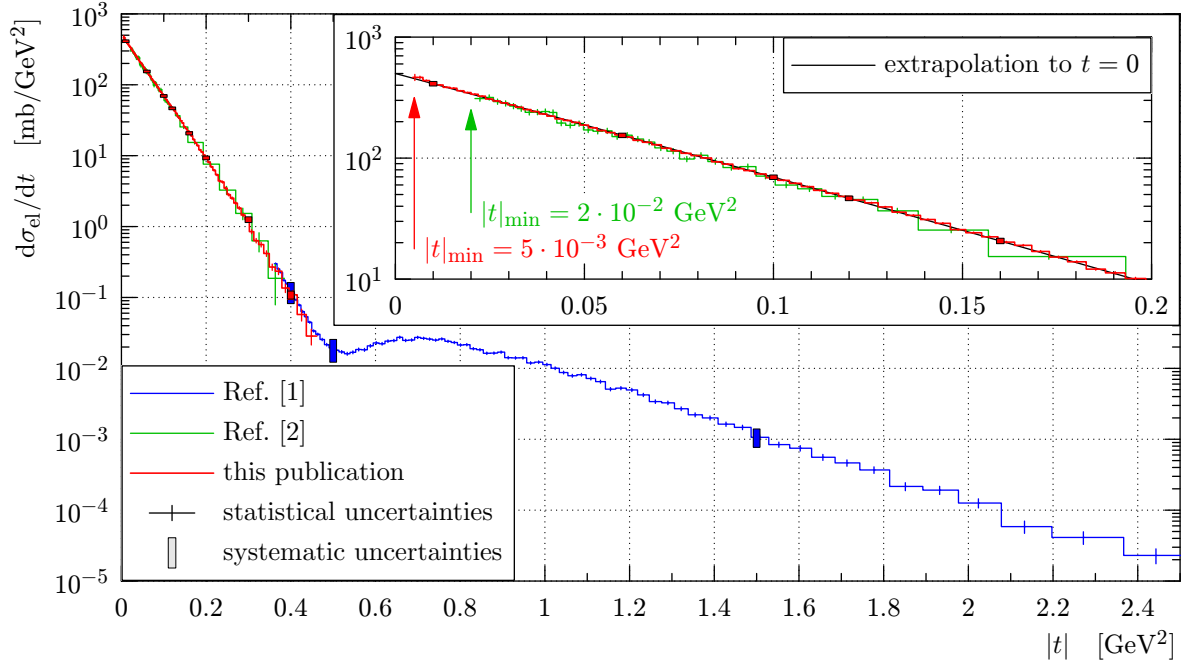
In order to derive the elastic and total cross-sections, the extrapolation to the optical point  $t = 0$  was performed (see Eq. (4)). The fact that 91% of the elastic cross-section was visible, gives high confidence to the derived cross-sections, all summarized in Tab. 7 with their statistical and systematic uncertainties. The elastic data were integrated up to  $|t| = 0.415\text{GeV}^2$ , where the effect of the larger  $|t|$ -contributions is small compared to the other uncertainties. The optical theorem can be used to calculate the total and inelastic cross-sections:

$$\sigma_{\text{tot}}^2 = \frac{16\pi(\hbar c)^2}{1 + \rho^2} \left. \frac{d\sigma_{el}}{dt} \right|_0, \quad \sigma_{\text{inel}} = \sigma_{\text{tot}} - \sigma_{el}. \quad (5)$$

For the  $\rho$  parameter the COMPETE [11] preferred-model extrapolation of  $0.141 \pm 0.007$  was chosen.

**Table 5:** The elastic differential cross-section as given in [1]. The systematic uncertainties are almost fully correlated among the bins.

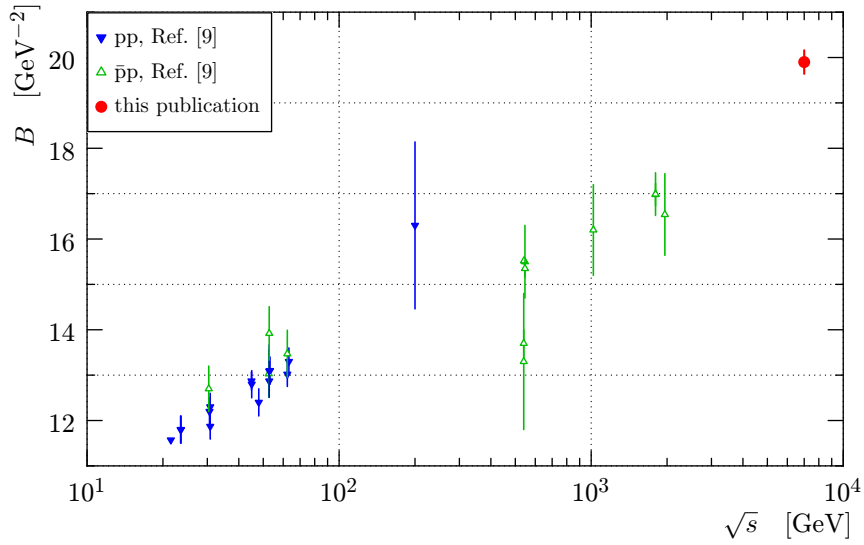
$ t $ [GeV <sup>2</sup> ]	$\frac{d\sigma_{el}}{dt}$ [ $\mu\text{b}/\text{GeV}^2$ ]	$ t $ [GeV <sup>2</sup> ]	$\frac{d\sigma_{el}}{dt}$ [ $\mu\text{b}/\text{GeV}^2$ ]	$ t $ [GeV <sup>2</sup> ]	$\frac{d\sigma_{el}}{dt}$ [ $\mu\text{b}/\text{GeV}^2$ ]	$ t $ [GeV <sup>2</sup> ]	$\frac{d\sigma_{el}}{dt}$ [ $\mu\text{b}/\text{GeV}^2$ ]
	$\pm\text{stat}\pm\text{syst}$		$\pm\text{stat}\pm\text{syst}$		$\pm\text{stat}\pm\text{syst}$		$\pm\text{stat}\pm\text{syst}$
0.377±0.002	225. ±6. ±55.8	0.574±0.004	18.3±0.9±5.1	0.863±0.005	16.3±0.6±4.5	1.290±0.009	3.3 ±0.2 ±1.0
0.384±0.002	174. ±5. ±43.3	0.588±0.004	20.8±0.9±7.0	0.880±0.005	16.4±0.6±5.8	1.322±0.009	2.7 ±0.2 ±0.7
0.391±0.002	157. ±4. ±39.6	0.602±0.004	22.8±1.0±8.7	0.897±0.005	16.9±0.6±4.7	1.355±0.010	2.2 ±0.1 ±0.6
0.398±0.002	133. ±4. ±33.4	0.616±0.004	22.2±1.0±6.2	0.913±0.005	14.1±0.6±3.9	1.390±0.011	2.0 ±0.1 ±0.5
0.405±0.002	116. ±3. ±29.9	0.629±0.004	24.2±1.0±8.8	0.931±0.005	14.0±0.6±3.9	1.428±0.011	1.6 ±0.1 ±0.4
0.412±0.002	93. ±3. ±24.3	0.643±0.004	24.7±1.0±6.9	0.948±0.005	14.1±0.6±4.9	1.467±0.011	1.5 ±0.1 ±0.4
0.420±0.002	78. ±2. ±20.3	0.657±0.004	27.4±1.1±7.6	0.966±0.005	11.9±0.5±3.3	1.507±0.012	1.1 ±0.1 ±0.3
0.428±0.002	63. ±2. ±16.2	0.671±0.004	24.8±1.0±9.3	0.985±0.006	12.2±0.5±4.1	1.552±0.014	0.84 ±0.07 ±0.23
0.436±0.002	54. ±2. ±14.0	0.685±0.004	25.1±1.0±7.0	1.005±0.006	11.3±0.5±3.1	1.603±0.015	0.75 ±0.07 ±0.20
0.445±0.003	45. ±1. ±12.2	0.700±0.004	27.3±1.0±7.6	1.024±0.006	10.0±0.4±2.8	1.656±0.016	0.56 ±0.05 ±0.15
0.454±0.003	34. ±1. ±9.9	0.714±0.004	26.5±1.0±9.8	1.044±0.006	8.7±0.4±3.0	1.713±0.017	0.46 ±0.05 ±0.13
0.464±0.003	30. ±1. ±12.8	0.728±0.004	25.9±1.0±7.2	1.065±0.006	7.9±0.4±2.2	1.777±0.020	0.37 ±0.04 ±0.10
0.474±0.003	26. ±1. ±10.7	0.742±0.004	25.0±0.9±9.2	1.086±0.006	8.1±0.4±2.2	1.851±0.023	0.22 ±0.03 ±0.06
0.485±0.003	21.6±0.9±5.9	0.757±0.004	26.0±0.9±7.2	1.108±0.006	7.2±0.3±2.0	1.932±0.024	0.19 ±0.03 ±0.05
0.496±0.003	19.5±0.9±7.6	0.771±0.004	24.1±0.9±8.8	1.131±0.007	6.5±0.3±1.8	2.024±0.029	0.13 ±0.02 ±0.03
0.508±0.003	18.0±0.8±5.0	0.786±0.004	23.2±0.8±6.4	1.155±0.007	5.1±0.3±1.4	2.133±0.034	0.059 ±0.012 ±0.015
0.520±0.004	17.1±0.8±4.8	0.801±0.004	21.3±0.8±5.9	1.179±0.007	5.3±0.3±1.4	2.272±0.048	0.041 ±0.008 ±0.011
0.533±0.004	16.1±0.8±6.6	0.816±0.004	21.6±0.8±6.0	1.205±0.008	5.0±0.3±1.7	2.443±0.050	0.023 ±0.005 ±0.006
0.547±0.004	16.9±0.8±4.7	0.831±0.004	18.9±0.7±5.2	1.232±0.008	4.2±0.2±1.2		
0.560±0.004	18.5±0.9±5.2	0.847±0.005	18.3±0.7±5.1	1.261±0.008	3.4±0.2±0.9		



**Fig. 2:** The elastic differential cross-section measurements by TOTEM. Each measurement is shown in a different color. The embedded figure provides a zoom of the region used for extrapolation to  $t = 0$ , showing the lowest  $|t|$ -values accessible in the analysis from Ref. [2] (green) and this analysis (red).

**Table 6:** Elastic slopes  $B$  (in  $\text{GeV}^{-2}$ ) obtained from parameterization Eq. (4) fitted through intervals  $|t|_{\text{low}}$  to  $|t|_{\text{high}}$ .

	$ t _{\text{low}}$	$ t _{\text{high}}$
	$0.1\text{ GeV}^2$	
	$0.2\text{ GeV}^2$	
$0.005\text{ GeV}^2$	$19.96 \pm 0.04^{\text{stat}} \pm 0.22^{\text{syst}}$	$19.89 \pm 0.02^{\text{stat}} \pm 0.27^{\text{syst}}$
$0.020\text{ GeV}^2$	$19.93 \pm 0.05^{\text{stat}} \pm 0.21^{\text{syst}}$	$19.87 \pm 0.03^{\text{stat}} \pm 0.33^{\text{syst}}$

**Fig. 3:** The elastic slope  $B$  (see Eq. (4)) as a function of the scattering energy  $\sqrt{s}$  (data from [9] use different treatments of the Coulomb-hadronic interference).**Table 7:** Result summary with detailed uncertainty composition. The  $t$ -dependent, normalization and luminosity uncertainties correspond to those presented in Tab. 3. The  $\rho$  uncertainty follows from the COMPETE preferred-model  $\rho$  extrapolation error of  $\pm 0.007$ . The right-most column gives the full systematic uncertainty, combined in quadrature and considering the correlations between the contributions (e.g. the uncertainty of  $\sigma_{\text{inel}}$  is suppressed due to the correlation between  $\sigma_{\text{el}}$  and  $d\sigma_{\text{el}}/dt|_0$ ).

quantity	value	statistical uncertainty	systematic uncertainty			
			$t$ -dep	norm	lumi	$\rho \Rightarrow$ full
$d\sigma_{\text{el}}/dt _0$ [mb/GeV <sup>2</sup> ]	506.4	$\pm 0.9$	$\pm 8.6$	$\pm 6.1$	$\pm 20.4$	$\Rightarrow \pm 23.0$
$B$ [GeV <sup>-2</sup> ]	19.89	$\pm 0.03$	$\pm 0.27$			$\Rightarrow \pm 0.27$
$\sigma_{\text{el}}$ [mb]	25.43	$\pm 0.03$	$\pm 0.10$	$\pm 0.31$	$\pm 1.02$	$\Rightarrow \pm 1.07$
$\sigma_{\text{tot}}$ [mb]	98.58		$\pm 0.84$	$\pm 0.59$	$\pm 1.98$	$\pm 0.10 \Rightarrow \pm 2.23$
$\sigma_{\text{inel}}$ [mb]	73.15		$\pm 0.77$	$\pm 0.29$	$\pm 0.96$	$\pm 0.10 \Rightarrow \pm 1.26$

## 9 Outlook

The above measurements will be repeated this year at the energy of  $\sqrt{s} = 8\text{TeV}$ . Furthermore, in the spirit of the 90m optics, a larger  $\beta^*$  optics ( $\beta^* = 500$  to 1000m) is presently under development. With such an optics at the energy of  $\sqrt{s} = 8\text{TeV}$ , minimum reachable  $|t|$ -values around  $5 \cdot 10^{-4}\text{GeV}^2$  (where Coulomb and hadronic contributions to the differential cross-sections are about equal) will allow the study of the Coulomb-hadronic interference and consequently the determination of the  $\rho$  parameter. Likewise, measurements of large  $|t|$  elastic scattering are under study. Such measurements might reveal further diffractive minima as predicted by some phenomenological models.

## Acknowledgements

We are indebted to the beam optics development team for the design, the thorough preparations and the successful commissioning of the  $\beta^* = 90\text{m}$  optics. We congratulate the CERN accelerator groups for the very smooth operation in 2011. We thank the LHC machine coordinators for scheduling the dedicated fills.

We are grateful to CMS for providing their luminosity measurements.

This work was supported by the institutions listed on the front page and partially also by NSF (US), the Magnus Ehrnrooth foundation (Finland), the Waldemar von Frenckell foundation (Finland), the Academy of Finland, the OTKA grant NK 101438, 73143 (Hungary) and the NKTH-OTKA grant 74458 (Hungary).

## References

- [1] ANTCHÉV G. *et al.* (TOTEM COLLABORATION), *Europhys. Lett.* **95** (2011) 41001
- [2] ANTCHÉV G. *et al.* (TOTEM COLLABORATION), *Europhys. Lett.* **96** (2011) 21002
- [3] ANTCHÉV G. *et al.* (TOTEM COLLABORATION), *Europhys. Lett.* **101** (2013) 21003
- [4] ANTCHÉV G. *et al.* (TOTEM COLLABORATION), *Europhys. Lett.* **101** (2013) 21004
- [5] ANELLI G. *et al.* (TOTEM COLLABORATION), *JINST* **3** (2008) S08007
- [6] KAŠPAR J., PhD Thesis, CERN-THESIS-2011-214, <http://cdsweb.cern.ch/record/1441140>
- [7] DEILE M., *The First 1 1/2 Years of TOTEM Roman Pot Operation at LHC*, in *Proceedings of the 2nd International Particle Accelerator Conference (IPAC 2011), San Sebastian, Spain*. arXiv:1110.5808v1
- [8] KAŠPAR, J. *et al.*, *Nucl. Phys.* **B843** (2011) 84
- [9] ISR (CR COLLABORATION), *Phys. Lett.* **B62** (1976) 460; ISR (ACHGT COLLABORATION), *Phys. Lett.* **B39** (1972) 663; ISR (R-211), *Nucl. Phys.* **B262** (1985) 689; ISR (R-210), *Phys. Lett.* **B115** (1982) 495; UA1, *Phys. Lett.* **B147** (1984) 385; UA4, *Phys. Lett.* **B127** (1983) 472 and *Phys. Lett.* **B198** (1987) 583; UA4/2, *Phys. Lett.* **B316** (1993) 448; CDF, *Phys. Rev.* **D50** (1994) 5518; E710, *Phys. Rev. Lett.* **68** (1992) 2433 and *Nuovo Cimento* **A106** (1992) 123; D0, D0 Note 6056-CONF; PP2PP, *Phys. Lett.* **B579** (2004) 245
- [10] LAFFERTY G. D. AND WYATT T. R., *Nucl. Instrum. Meth. A* **355** (1995) 541
- [11] CUDELL J. R. *et al.* (COMPETE COLLABORATION), *Phys. Rev. Lett.* **89** (2002) 201801